Instantaneous insulation in a micro-slab: A mechanism for flow generation in a rarefied gas

A. Manela[1,*] and L. Pogorelyuk[2]

[1]*Faculty of Aerospace Engineering, Technion–Israel Institute of Technology, Haifa 32000, Israel*
[2]*Department of Mechanical and Aerospace Engineering, Princeton University,*
Princeton, New Jersey 08544, USA

We analyze the response of a gas in a micro-slab, set at an initial pure-conduction state, to instantaneous thermal insulation of its boundaries. In line with ongoing efforts in generating gas flows at the microscale, thermal insulation is suggested as a means for flow excitation with no moving parts. The problem is analyzed in the entire range of gas rarefaction rates and for arbitrary initial temperature differences between the walls. Analytical solutions are obtained in the linearized limit of small temperature differences for large (collisionless) and small (continuum) Knudsen numbers. These solutions are supported by direct simulation Monte Carlo calculations, which are then used to investigate the nonlinear problem with large initial temperature differences. Followed by the system's initial state, boundary insulation results in a series of time-decaying waves, propagating across the slab, and transferring the system between its conductive and adiabatic equilibrium states. While larger initial temperature differences result in higher flow rates, it is found that nonlinear effects reduce the efficiency of flow excitation through boundaries insulation. At high Knudsen numbers, this is rationalized through the system's initial state, in which the gas uniform temperature is lower than the arithmetic mean of walls temperatures. At low Knudsen numbers, the dominant effect of molecular collisions causes thermal dissipation, which in turn results in kinetic energy losses. The analysis may be readily applied to calculate the gas response to arbitrary time variations of the boundary-imposed heat flux.

I. INTRODUCTION

Ongoing developments in the field of micro-electro-mechanical systems require continuous investigations of microfluidic flows, for both liquids and gases [1]. At the very small length scales considered, the excitation and control of such flows are particularly challenging and are the focus of a large number of studies. These works have led to the invention of microscale pumps [2] and mixers [3], used in a variety of biomedical applications [4]. Traditionally, the flow actuators developed thereof may be of active or passive type. In active actuators, the flow is excited through mechanically moving components, such as pistons and thin films. In passively excited flows, no moving parts are involved, but are replaced by nonmechanical flow-induction methodologies. This has the clear advantage of avoiding mechanical wear caused by component motion.

Focusing on passive flow excitation in rarefied gases, the concept of Knudsen pumps was introduced by Maxwell [5] during the nineteenth century and studied ever since (see, e.g., [6], and references cited therein). In this setup, gas motion parallel to a surface is induced by a temperature gradient along the boundary. In a concurrent set of works, it was found that time-dependent temperature changes at a boundary induce gas motion in its normal direction. Specifically, the response of a gas to instantaneous [7–9] and continuous [10] time temperature changes has been investigated. Common to these works is the consideration of linearized conditions of small

---

*Corresponding author: amanela@technion.ac.il

temperature variations and the direct application of temperature boundary conditions at the walls. The latter, however, appears of little practical value, as the surface temperature at any experimental setup can only be prescribed indirectly through the direct imposition of boundary heat flux. Thus, apart from the fundamental interest in investigating the effect of heat-flux boundary conditions on the resulting flow, it is also of evident practical importance.

Noting the above in a more general context, the impact of replacing isothermal with heat-flux boundary conditions has been considered in several works. Gospodinov *et al.* [11] have investigated the impact of changing between isothermal and adiabatic conditions on the oscillatory cylindrical Couette flow developed at high rotation speeds. The work has demonstrated a nonlinear effect of heat transfer at nonsmall rotation velocities, resulting in deviations from the incompressible solution. In a different setup, Manela and Pogorelyuk [12,13] have considered the effect of thermal boundary conditions on the passage of sound waves in a rarefied gas. The results obtained have suggested a potential thermoacoustic mechanism for active noise control of a vibrating surface in the entire range of gas rarefaction levels. Most recently, Meng *et al.* [14] have studied numerically the effect of heat-flux boundary conditions on rarefied Couette and force-driven Poiseuille flows. Their work showed that a zero-heat-flux (adiabatic) wall may significantly influence the flow at high speeds.

The objective of the present work is to extend existing analyses on the response of a rarefied gas to unsteady changes in the thermal properties of its boundaries. The main differences from previous investigations are: (i) Boundary conditions on wall temperatures are replaced by conditions on the normal heat flux. The boundary temperature is thus treated as unknown and is calculated in the process of analysis. Apart from being a more realistic representation, it is indeed the change in surface heat flux, rather than in its temperature, that is the physical source for gas motion. (ii) An initial equilibrium state of pure conduction, i.e., with nonzero uniform heat flux, is considered. This is qualitatively different from the zero-heat-flux initial state taken in previous works. Apart from modifying the problem formulation and analysis, the consideration of a nonzero-heat-flux state enables investigation of the mechanism of small-scale energy transfer from gas thermal energy into kinetic energy. (iii) The problem is studied in both linear and nonlinear regimes, by considering arbitrary values of the walls' initial heat flux.

We consider a one-dimensional gas-in-a-slab setup. The gas layer is initially set in a pure-conduction equilibrium state with its confining walls fixed at different temperatures. The initial equilibrium state is governed by the (equal) normal heat-flux magnitudes imposed at the walls, the temperature of one of the walls (or, instead, the mean gas temperature), and the mean density of the gas. At time $t^* = 0$, the boundaries are thermally insulated and the gas response is followed through its terminal state. We analyze the problem in the entire range of gas rarefaction rates and for arbitrary magnitudes of initial heat flux. Thus, both linear and nonlinear problems are considered.

The paper is organized as follows. In Sec. II the general statement of the problem is given. The numerical scheme applied for analyzing the problem, the direct simulation Monte Carlo (DSMC) method, is discussed in Sec. III. In Sec. IV the linear problem of small initial heat fluxes is considered and comparison is made between numerical and analytical predictions in the collisionless and continuum limits. The nonlinear problem is investigated in Sec. V. A summary of our results and an assessment of their significance are given in Sec. VI.

II. STATEMENT OF THE PROBLEM

Consider a gas layer of mean density ρ_0^* confined between two stationary diffuse reflecting walls. The walls are placed at $x^* = \mp L^*/2$ in the (y^*, z^*) plane, with asterisks denoting dimensional quantities. At time $t^* < 0$, the wall at $x^* = -L^*/2$ is set at temperature $T^* = T_c^*$ and both walls are subject to uniform heat flux in the normal direction

$$\mathbf{q}_w^*(t^* < 0) = q_w^* \hat{\mathbf{x}}, \tag{1}$$

fixing the gas pure-conduction initial state. At time $t^* = 0$, the walls are instantaneously insulated and the system is kept adiabatic thereafter,

$$\mathbf{q}_w^*(t^* \geqslant 0) = \mathbf{0}. \tag{2}$$

In the following we investigate the transient system response to its thermal insulation and its relaxation towards the terminal adiabatic state in the entire range of gas rarefaction rates and initial heat-flux magnitudes q_w^*.

Before proceeding to problem analysis, scaling is introduced. We normalize the position and velocity by the slab width L^* and mean thermal speed $U_{\text{th}}^* = \sqrt{2R^* T_0^*}$, respectively. Here R^* marks the specific gas constant and the temperature T_0^* is the arithmetic mean of wall temperatures at the initial equilibrium state. This scale for the temperature appears useful for analyzing the linear problem, where symmetry properties of the system (about its mean equilibrium state) apply. The time is normalized by L^*/U_{th}^*. The temperature and density are nondimensionalized by T_0^* and ρ_0^*, respectively, and the heat flux is scaled by $\rho_0^* U_{\text{th}}^{*3}$. The resulting scaled problem is governed by the nondimensional parameters

$$q_w = q_w^*/\rho_0^* U_{\text{th}}^{*3}, \quad \text{Kn} = l^*/L^*, \tag{3}$$

denoting the initial wall heat-flux magnitude and gas Knudsen number (where l^* marks the mean free path of a gas molecule), respectively. In terms of the nondimensional formulation, we investigate the system response in the entire range of q_w and Kn. To start with, we focus on the linearized problem of small initial heat flux at the walls $q_w \ll 1$ and study the system response at ballistic (Kn $\gg 1$), continuum (Kn $\ll 1$), and intermediate [Kn $\sim O(1)$] conditions. We then consider the nonlinear problem, where $q_w \sim O(1)$, in the entire range of Knudsen numbers. The numerical scheme applied for the calculation is the DSMC method, to be discussed in the next section. Analytical predictions are made in the linearized limit, studied in Sec. IV, and, to a limited extent, also in the nonlinear case in Sec. V. These predictions are assessed through comparison with DSMC results, which are considered numerically exact.

III. NUMERICAL SCHEME: THE DSMC METHOD

The DSMC method is a stochastic particle method commonly used for studying rarefied gas flows, and is now accepted as the most reliable scheme for analyzing complex gas flows in the entire range of noncontinuum conditions [15]. In the present work, a one-dimensional version of the DSMC scheme is employed to analyze the system response. We consider a hard-sphere gas collision model in a finite domain, in conjunction with the diffuse reflection model for gas-surface interactions. In common applications of the DSMC algorithm, such interactions are modeled through direct prescription of the wall temperatures. However, in the present work, heat-flux boundary conditions are applied instead, where the wall temperatures are treated as unknown. Towards this end, the temperatures of the walls at each simulation time step are controlled in a closed-loop manner, to reduce the deviations from the desired heat flux. The algorithm has been used previously by the present authors and is described in Ref. [12].

The numerical realization of the problem consists of two stages. Initially, the gas pure-conduction equilibrium distribution is achieved. Then the boundaries are turned adiabatic and the calculation follows the system evolution through its final equilibrium. In practice, any deviation from the initial pure-conduction state affects the initial system condition at the instant of wall insulation which, in turn modifies the transient system behavior at $t > 0$. It is therefore important to enable full system relaxation before the wall insulation is applied.

The scheme above may have been simplified considerably if the molecular description of the gas at the initial equilibrium was known for arbitrary Knudsen numbers. However, an explicit expression for the distribution of particle velocities is available only in the collisionless limit [16], while at finite and small Knudsen numbers only numerical approximations exist, even for linearized conditions (see, e.g., [17]). For simplicity, we have applied the molecular distribution for collisionless

conditions as the simulation's initial condition. This choice is nearly exact at high Knudsen numbers and thus resulted in short relaxation times of the system. Yet, with decreasing Knudsen number, the pure-conduction state deviates considerably from the collisionless distribution, resulting in increasing relaxation times. In all cases, system equilibration has been ensured by monitoring the fluctuations in all macroscopic fields and verifying that they decay below the statistical noise level before switching the boundary conditions.

In line with the discussion in Sec. II, DSMC calculations were carried out for both linear ($q_w \ll 1$) and nonlinear [$q_w \sim O(1)$] setups. In the former case, simulation results are characterized by high noise levels, resulting from the statistical scattering inherent in the computational algorithm. This has been resolved through repeated time averaging of the signal. The domain was split into 128 computational cells and 256 subcells. The time step applied was 1/3 of the cell length over the gas thermal speed at equilibrium. To resolve the statistical scattering mentioned above, the numerical results were averaged over 16 time steps (roughly five computational cell lengths over the gas thermal speed at equilibrium), ensuring sufficiently low noise levels that enable comparison between the numerical and analytical predictions. A typical calculation required an order of 5×10^7 DSMC particles to allow for numerical convergence.

IV. LINEARIZED PROBLEM

We start by considering the linearized problem, where the initial heat-flux magnitude q_w (and consequent temperature difference between the walls) is small. The problem is studied analytically in the limits of large (collisionless flow, Sec. IV A) and small (continuum limit, Sec. IV B) Knudsen numbers. The Monte Carlo simulation discussed in Sec. III is used to validate the analytical predictions and characterize the breakdown of each limit with varying Kn. Our results are described in Sec. IV C

A. Ballistic-flow regime

When the slab width L^* is of the order of the mean free path or smaller, the continuum hypothesis does not apply and the molecular description of the gas must be taken into account. In the limit case of Kn $= l^*/L^* \gg 1$, the effect of gas molecular collisions may be neglected and the flow may be treated as ballistic. Making use of the kinetic theory of gases [18], the gas state is described by the velocity distribution function

$$f(x,t,\mathbf{c}) = F[1 + \varepsilon\phi(x,t,\mathbf{c})], \tag{4}$$

where $\mathbf{c} = (c_x,c_y,c_z)$ is the vector of molecular velocity and $F = \pi^{-3/2}\exp[-c^2]$ is the scaled equilibrium Maxwellian distribution. In the absence of molecular collisions, we consider the collisionless Boltzmann equation for $\phi(\mathbf{x},t,\mathbf{c})$,

$$\frac{\partial\phi}{\partial t} + c_x\frac{\partial\phi}{\partial x} = 0. \tag{5}$$

The equation is supplemented by wall boundary conditions, describing the interaction between the gas molecules and the surfaces. We consider purely diffuse boundaries [18], according to which the molecules reflected from the surfaces (having $c_x \gtrless 0$ at $x = \mp0.5$, respectively) acquire Maxwellian (equilibrium) distribution characterized by each of the walls' properties. In a linearized formulation,

$$\phi(x = \mp 1/2,t,c_x \gtrless 0,c_y,c_z) = \rho_\pm(t) + T_\pm(t)(c^2 - 3/2), \tag{6}$$

where $\rho_\pm(t)$ and $T_\pm(t)$ (the latter being the scaled time perturbation of the surfaces temperatures) need to be determined.

The above problem is analyzed by applying the time Fourier transform

$$\bar{G}(\omega) = \int_{-\infty}^{\infty} G(t)\exp[-i\omega t]dt \tag{7}$$

to Eqs. (5) and (6). This yields the transformed equation

$$i\omega\bar{\phi} + c_x \frac{d\bar{\phi}}{dx} = 0 \tag{8}$$

and boundary conditions

$$\bar{\phi}(x = \mp 1/2, \omega, c_x \gtrless 0, c_y, c_z) = \bar{\rho}_\pm(\omega) + \bar{T}_\pm(\omega)(c^2 - 3/2) \tag{9}$$

amenable to the solution

$$\bar{\phi}(x, \omega, c_x \gtrless 0, c_y, c_z) = [\bar{\rho}_\pm(\omega) + \bar{T}_\pm(\omega)(c^2 - 3/2)] \exp\left[-i\omega \frac{x \pm 1/2}{c_x}\right]. \tag{10}$$

The time-domain solution is obtained by taking the inverse Fourier transform

$$G(t) = \frac{1}{2\pi} \int_{-\infty}^{\infty} \bar{G}(\omega) \exp[i\omega t]d\omega \tag{11}$$

of Eq. (10), yielding

$$\phi(x, t, c_x \gtrless 0, c_y, c_z) = \rho_\pm(t_\pm) + T_\pm(t_\pm)(c^2 - 3/2), \tag{12}$$

where $t_\pm = t - (x \pm 1/2)/c_x$.

The fields $\rho_\pm(t)$ and $T_\pm(t)$ appearing in Eq. (12) are specified by imposing the macroscopic impermeability and heat-flux wall conditions [18]

$$\frac{1}{\pi^{3/2}} \int_{-\infty}^{\infty} c_x \phi(x = \mp 1/2) \exp[-c^2]d\mathbf{c} = 0 \tag{13}$$

and

$$\frac{1}{2\pi^{3/2}} \int_{-\infty}^{\infty} c^2 c_x \phi(x = \mp 1/2) \exp[-c^2]d\mathbf{c} = q_w[1 - H(t)], \tag{14}$$

respectively. In Eq. (14), $H(t)$ denotes the Heaviside step function, marking the instantaneous insulation of the walls at $t = 0$ [see Eqs. (1) and (2)]. Problem symmetry (imposed by the symmetry in wall boundary conditions and the scaling introduced) sets

$$\rho_-(t) = -\rho_+(t), \quad T_-(t) = -T_+(t) \tag{15}$$

and it is therefore required to satisfy conditions (13) and (14) at one boundary only. At the prior-to-insulation ($t < 0$) pure-conduction state, substitution of Eq. (12) into Eqs. (13) and (14) yields

$$\rho_\pm(t < 0) = \pm q_w \sqrt{\pi}/2, \quad T_\pm(t < 0) = \mp q_w \sqrt{\pi}, \tag{16}$$

which fixes the gas state (12) at the initial equilibrium. Consequently, the initial macroscopic perturbations of temperature, density, pressure, and normal heat flux are given by

$$T(x, t < 0) = \rho(x, t < 0) = p(x, t < 0) = 0, \quad q(x, t < 0) = q_w, \tag{17}$$

respectively.

To obtain the transient system response after boundaries insulation, we substitute Eq. (12) into Eqs. (13) and (14) with $t \geqslant 0$. Imposing the boundary conditions at $x = -1/2$ together with (15) and applying the change of variables $\tau = t + 1/c_x$, we obtain a system of nonhomogeneous integral equations for $\rho_+(t \geqslant 0)$ and $T_+(t \geqslant 0)$,

$$\rho_+(t) + \frac{1}{2}T_+(t) + 2 \int_0^t \frac{\rho_+(\tau)}{(t-\tau)^3} \exp[-(t-\tau)^{-2}]d\tau$$

$$+ \int_0^t \frac{T_+(\tau)}{(t-\tau)^3} \left[\frac{2}{(t-\tau)^2} - 1\right] \exp[-(t-\tau)^{-2}]d\tau = \frac{q_w\sqrt{\pi}}{t^2} \exp[-t^{-2}] \tag{18}$$

and

$$\rho_+(t) + \frac{3}{2}T_+(t) + \int_0^t \frac{\rho_+(\tau)}{(t-\tau)^3}\left[\frac{1}{(t-\tau)^2} + 1\right]\exp[-(t-\tau)^{-2}]d\tau$$
$$+ \int_0^t \frac{T_+(\tau)}{(t-\tau)^3}\left[\frac{1}{(t-\tau)^4} + \frac{1}{2(t-\tau)^2} + \frac{1}{2}\right]\exp[-(t-\tau)^{-2}]d\tau$$
$$= q_w\sqrt{\pi}\left[\exp[-t^{-2}]\left(\frac{1}{2t^4} + \frac{1}{t^2} + 1\right) - 1\right]. \tag{19}$$

The system of equations satisfies the initial conditions set by the initial equilibrium state [see Eqs. (12) and (16)] at $t = 0^-$. The forcing terms appearing on the right-hand side in Eqs. (18) and (19) originate from the contribution of molecules reflected from the $x = +1/2$ boundary at time $t < 0$ and are thus proportional to q_w. These terms vanish at $t \gg 1$, where the system resumes its final equilibrium state

$$T(x, t \gg 1) = \rho(x, t \gg 1) = p(x, t \gg 1) = q(x, t \gg 1) = 0, \tag{20}$$

which differs from the uniform initial equilibrium (17) by the value of the heat flux. It is this difference between the conductive and adiabatic equilibrium states that drives the nonzero gas flow at the transient time interval.

To solve for $\rho_+(t)$ and $T_+(t)$ at $t \geqslant 0$, Eq. (19) is subtracted from Eq. (18) to yield

$$T_+(t) = -\int_0^t \frac{\rho_+(\tau)}{(t-\tau)^3}\left[\frac{1}{(t-\tau)^2} - 1\right]\exp[-(t-\tau)^{-2}]d\tau$$
$$- \int_0^t \frac{T_+(\tau)}{(t-\tau)^3}\left[\frac{1}{(t-\tau)^4} - \frac{3}{2(t-\tau)^2} + \frac{3}{2}\right]\exp[-(t-\tau)^{-2}]d\tau$$
$$+ q_w\sqrt{\pi}\left[\left(\frac{1}{2t^4} + 1\right) - 1\right]\exp[-t^{-2}]. \tag{21}$$

Starting with $t = 0$, where the initial conditions (16) apply, $T_+(t)$ is calculated via time discretization and numerical evaluation of the right-hand side of Eq. (21).[1] Once $T_+(t)$ is calculated at each time step, evaluation of $\rho_+(t)$ follows from its isolation from Eqs. (18) or (19).

With $\rho_+(t)$ and $T_+(t)$ known, the probability density perturbation ϕ in Eq. (12) is determined and the $O(\varepsilon)$ perturbations of the hydrodynamic fields are computed through appropriate quadratures over the space of molecular velocities [18]. Defining

$$J_\pm^n(x,t) = \int_0^{\pm\infty} \rho_\pm(t_\pm)c_x^n\exp\left[-c_x^2\right]dc_x, \quad K_\pm^n(x,t) = \int_0^{\pm\infty} T_\pm(t_\pm)c_x^n\exp\left[-c_x^2\right]dc_x, \tag{22}$$

the expressions for the density, velocity, pressure, and heat-flux fields are given by

$$\rho(x,t) = \frac{1}{\sqrt{\pi}}\left[J_+^0 - J_-^0 + K_+^2 - K_-^2 - \frac{1}{2}(K_+^0 - K_-^0)\right], \tag{23}$$

$$u(x,t) = \frac{1}{\sqrt{\pi}}\left[J_+^1 - J_-^1 + K_+^3 - K_-^3 - \frac{1}{2}(K_+^1 - K_-^1)\right], \tag{24}$$

$$p(x,t) = \frac{2}{3\sqrt{\pi}}\left[J_+^2 - J_-^2 + J_+^0 - J_-^0 + K_+^4 - K_-^4 - \frac{1}{2}(K_+^2 - K_-^2) - \frac{1}{2}(K_+^0 - K_-^0)\right], \tag{25}$$

---

[1]Note that, at a given time $t > 0$, such evaluation requires the values of ρ_+ and T_+ at times $\tau < t$ only, since both integrands on the right-hand side of Eq. (21) vanish at $\tau = t$.

and

$$q(x,t) = -\frac{5}{4}u + \frac{1}{2\sqrt{\pi}}\left[J_+^3 - J_-^3 + J_+^1 - J_-^1 + K_+^5 - K_-^5 - \frac{1}{2}(K_+^3 - K_-^3) - \frac{1}{2}(K_+^1 - K_-^1)\right],$$
(26)

respectively. The temperature perturbation is obtained by the linearized form of the gas equation of state

$$T = p - \rho.$$
(27)

To evaluate of $J_\pm^n(x,t)$ and $K_\pm^n(x,t)$ in Eqs. (23)–(26), the integral expressions in Eq. (22) are divided into

$$J_\pm^n(x,t) = \mp\frac{q_w\sqrt{\pi}}{2}\int_0^{(x\pm 1/2)/t} c_x^n \exp\left[-c_x^2\right]dc_x \pm \int_0^t \rho_+(\tau)\frac{(x\pm 1/2)^{n+1}}{(t-\tau)^{n+2}}\exp\left[-\left(\frac{x\pm 1/2}{t-\tau}\right)^2\right]d\tau,$$

$$K_\pm^n(x,t) = \pm q_w\sqrt{\pi}\int_0^{(x\pm 1/2)/t} c_x^n \exp\left[-c_x^2\right]dc_x \pm \int_0^t T_+(\tau)\frac{(x\pm 1/2)^{n+1}}{(t-\tau)^{n+2}}\exp\left[-\left(\frac{x\pm 1/2}{t-\tau}\right)^2\right]d\tau.$$
(28)

In Eq. (28) the explicitly calculated integrals multiplied by q_w reflect the cumulative effect of gas molecules whose recent collision with a boundary occurred at $t < 0$. With increasing time, the upper limit of these integrals decreases and their contribution vanishes. The integrals containing $\rho_+(\tau)$ and $T_+(\tau)$, contributed by molecules whose recent collision with a boundary occurred after $t = 0$, are evaluated numerically, based on the numerical calculation of $\rho_+(\tau)$ and $T_+(\tau)$ described above.

The ballistic-flow approximation is expected to hold in all cases where Kn $\gg$ 1. Additionally, since the time scale characterizing the change in boundary conditions is exceedingly small, it may be expected that the collisionless approximation describes well the short-time gas response at nonlarge Knudsen numbers when $t \lesssim$ Kn (or, in dimensional notation, $t^* \lesssim l^*/U_{th}^*$). This will be examined in the results of Sec. IV C.

B. Continuum model

Assuming that the distance L^* between the boundaries is much larger than the mean free path l^*, continuum conditions prevail and the Navier-Stokes-Fourier equations may be applied to obtain the system behavior. Making use of the scaling introduced in Sec. II and linearizing about the initial equilibrium state, we obtain the $O(\varepsilon)$ unsteady one-dimensional balances of mass, momentum, and energy

$$\frac{\partial\rho}{\partial t} + \frac{\partial u}{\partial x} = 0, \quad \frac{\partial u}{\partial t} = -\frac{1}{2}\left(\frac{\partial\rho}{\partial x} + \frac{\partial T}{\partial x}\right) + \frac{4\widetilde{Kn}}{3}\frac{\partial^2 u}{\partial x^2}, \quad \frac{\partial T}{\partial t} = \frac{\gamma\widetilde{Kn}}{Pr}\frac{\partial^2 T}{\partial x^2} - (\gamma-1)\frac{\partial u}{\partial x}, \quad (29)$$

respectively. The $O(\varepsilon)$ pressure perturbation and normal heat flux are given by the linearized form of the equation of state and Fourier's law

$$p = \rho + T, \quad q = -\beta\frac{\partial T}{\partial x},$$
(30)

respectively. In Eqs. (29) and (30),

$$\widetilde{Kn} = \frac{\mu_0^*}{\rho_0^* U_{th}^* l^*}, \quad Pr = \frac{\mu_0^* c_p^*}{k_0^*}, \quad \gamma = \frac{c_p^*}{c_v^*}, \quad \beta = \frac{k_0^* T_0^*}{\rho_0^* U_{th}^{*3} L^*},$$
(31)

where μ_0^* and k_0^* denote the coefficients of gas dynamic viscosity and thermal conductivity at the temperature T_0^*, respectively, and c_p^* and c_v^* mark the gas specific heat capacities at constant pressure and volume, respectively. For the perfect hard-sphere gas considered here, the Prandtl number

$\mathrm{Pr} = 2/3$ and $\gamma = 5/3$. In addition, $\widetilde{\mathrm{Kn}} = (5\sqrt{\pi}/16)\mathrm{Kn}$ and $\beta = 15\widetilde{\mathrm{Kn}}/8$ [19]. The problem is supplemented by the boundary conditions of wall impermeability and prescribed heat flux

$$u = 0, \quad -\beta \frac{\partial T}{\partial x} = q_w[1 - H(t)] \quad \text{at } x = \mp 1/2, \tag{32}$$

respectively.

To analyze the problem, the time Fourier transform (7) is applied to Eqs. (29) and (32). This yields a system of ordinary equations

$$i\omega\bar{\rho} + \bar{u}' = 0, \quad i\omega\bar{u} = -\frac{1}{2}(\bar{\rho}' + \bar{T}') + \frac{4\widetilde{\mathrm{Kn}}}{3}\bar{u}'', \quad i\omega\bar{T} = \frac{\gamma\widetilde{\mathrm{Kn}}}{\mathrm{Pr}}\bar{T}'' - (\gamma - 1)\bar{u}' \tag{33}$$

accompanied by the boundary conditions

$$\bar{u}(\mp 1/2) = 0, \quad -\beta\bar{T}'(\mp 1/2) = q_w[\pi\delta(\omega) + i/\omega]. \tag{34}$$

Here a prime denotes differentiation with respect to x and δ denotes the Dirac delta function. Eliminating the density and velocity perturbations in Eq. (33) and substituting $\mathrm{Pr} = 2/3$ and $\gamma = 5/3$, we obtain a single equation for the temperature

$$a_2\bar{T}'''' + a_1\bar{T}'' + a_0\bar{T} = 0, \tag{35}$$

where

$$a_2 = \frac{5\widetilde{\mathrm{Kn}}}{2}\left(\frac{4\widetilde{\mathrm{Kn}}}{3\alpha} - \frac{i}{2\omega}\right), \quad a_1 = -\frac{1}{6}(23i\omega\widetilde{\mathrm{Kn}} + 5), \quad a_0 = -\omega^2. \tag{36}$$

The equation is supplemented by the four boundary conditions

$$c_1\bar{T}'''(\mp 1/2) + c_2\bar{T}'(\mp 1/2) = 0, \quad -\beta\bar{T}'(x = \mp 1/2) = q_w[\pi\delta(\omega) + i/\omega], \tag{37}$$

where

$$c_1 = -\frac{15\widetilde{\mathrm{Kn}}}{4\omega}\left(\frac{1}{2\omega} + \frac{4i\widetilde{\mathrm{Kn}}}{3}\right), \quad c_2 = \frac{5i}{4\omega} - 2\widetilde{\mathrm{Kn}}. \tag{38}$$

In line with the symmetry properties of the problem, $\bar{T}(x) = -\bar{T}(-x)$. The general solution for the Fourier-transformed temperature perturbation is then

$$\bar{T}(x,\omega) = A(\omega)\sinh[r_1(\omega)x] + B(\omega)\sinh[r_2(\omega)x], \tag{39}$$

where

$$r_{1,2}(\omega) = \left(\frac{-a_1 \pm \sqrt{a_1^2 - 4a_2a_0}}{2a_2}\right)^{1/2} \tag{40}$$

are the roots of the characteristic equation corresponding to Eq. (35). Making use of the boundary conditions (37) sets

$$A(\omega) = \frac{q_w[\pi\delta(\omega) + i/\omega]}{\beta[r_1\cosh(-r_1/2) + c_3r_2\cosh(-r_2/2)]}, \quad B(\omega) = c_3A(\omega), \tag{41}$$

where

$$c_3 = -\frac{r_1(c_1r_1^2 + c_2)\cosh(-r_1/2)}{r_2(c_1r_1^2 + c_2)\cosh(-r_2/2)}. \tag{42}$$
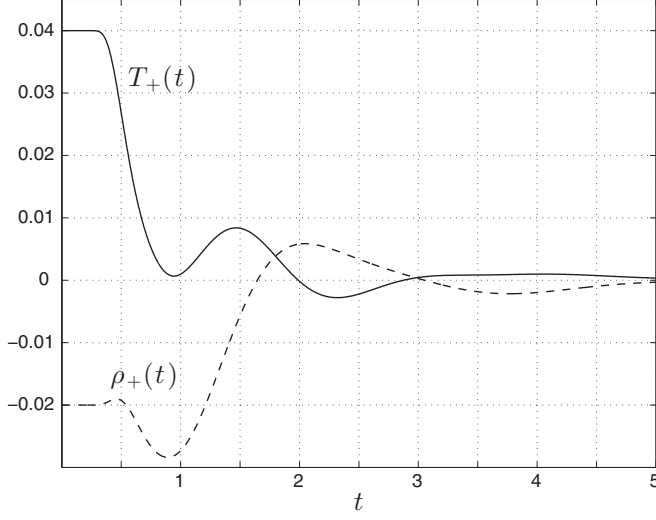
FIG. 1. Variations of $\rho_+(t)$ (dashed line) and $T_+(t)$ (solid line) in the collisionless solution for $q_w = -0.04/\sqrt{\pi}$.

Applying Eqs. (33) and (30), the transformed velocity, density, and heat-flux perturbations are given by

$$\bar{u}(x,\omega) = Ar_1\left(c_1 r_1^2 + c_2\right)\cosh(r_1 x) + Br_2\left(c_1 r_2^2 + c_2\right)\cosh(r_2 x),$$

$$\bar{\rho}(x,\omega) = \frac{i}{\omega}\left[Ar_1^2\left(c_1 r_1^2 + c_2\right)\sinh(r_1 x) + Br_2^2\left(c_1 r_2^2 + c_2\right)\sinh(r_2 x)\right], \qquad (43)$$

$$\bar{q}(x,\omega) = -\beta[Ar_1 \cosh(r_1 x) + Br_2 \cosh(r_2 x)],$$

respectively, and $\bar{p} = \bar{\rho} + \bar{T}$.

The time-domain description of the system is obtained by taking the real part of the inverse Fourier transform (11) of (43). The solution should describe the pure-conduction state of the system for $t < 0$ and the gas transient response for $t \geqslant 0$. The former equilibrium state may be obtained independently by solving the steady counterpart of Eqs. (29) and (32), yielding

$$T(x,t < 0) = -q_w x/\beta, \quad \rho(x,t < 0) = q_w x/\beta, \quad p(x,t < 0) = 0, \quad q(x,t < 0) = q_w. \qquad (44)$$

For later reference we also indicate the final equilibrium state of the system, given by the uniform distribution

$$T(x,t \gg 1) = \rho(x,t \gg 1) = p(x,t \gg 1) = q(x,t \gg 1) = 0, \qquad (45)$$

which is identical to the final equilibrium state in the collisionless limit (20). As discussed in Sec. V A, the two final states become different for nonlinear conditions, which affects the transient system behavior.

C. Results

We start by presenting the system response at large Knudsen numbers, analyzed in Sec. IV A. To describe the microscopic solution, Fig. 1 shows the time variations of ρ_+ and T_+, appearing in the collisionless solution (12), for $q_w = -0.04/\sqrt{\pi}$. The function $T_+(t)$ denotes the temperature deviation of the wall at $x = -1/2$ about the reference mean gas temperature. Using Eq. (16) for the present choice of q_w, $T_+(t < 0) = -0.04$ and $\rho_+(t < 0) = 0.02$. The results for $T_-(t)$ and $\rho_-(t)$ follow from the symmetry properties (15).
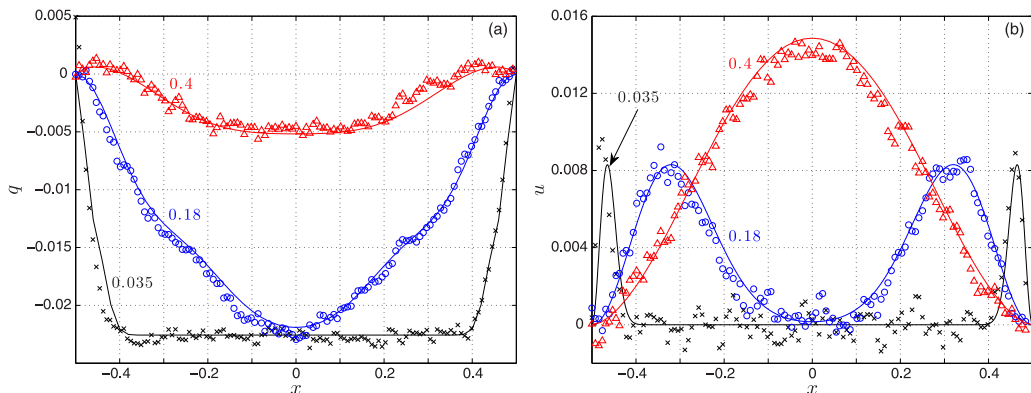
FIG. 2. x variations of the (a) normal heat flux and (b) velocity for $Kn \gg 1$ and $q_w \ll 1$ at early times: comparison between collisionless solution (solid lines) and DSMC predictions for $Kn = 20$ (symbols) at $t = 0.035$, 0.18, and 0.4 with $q_w = -0.04/\sqrt{\pi}$.

Considering the time interval $0 \leqslant t \leqslant 5$ presented in Fig. 1, we note that, at the instant $t = 0$ of boundaries insulation, T_+ and ρ_+ become discontinuous. Specifically, these functions acquire the initial equilibrium values of their counterpart $T_-(t < 0) = 0.04$ and $\rho_-(t < 0) = -0.02$ at the $x = 1/2$ wall [see Eq. (15)]. This is since, when insulated, each boundary accommodates the physical properties of the incoming particles, which in turn are governed by their recent collision with a boundary. At the initial time interval $0 \leqslant t \lesssim 0.5$, the walls interact almost entirely with molecules whose last wall collision occurred before $t = 0$. The $x = \mp 1/2$ wall properties are therefore interchanged and kept constant, with the $x = -1/2$ wall accommodating the properties of the $x = 1/2$ boundary (at $t < 0$) and vice versa. Yet the walls are not kept isothermal at later times, where particle-wall collisions occur with molecules whose previous wall interaction took place after $t = 0$. This results in the time variations shown in Fig. 1 for $t \gtrsim 0.5$. At late times $t \gtrsim 5$, both T_+ and ρ_+ vanish, indicating that the system has achieved its adiabatic equilibrium state [see Eq. (20)].

Focusing on the collisionless early-time response, Fig. 2 presents the x variations of the normal heat flux and velocity for $q_w = -0.04/\sqrt{\pi}$ at the indicated values of time. Both analytical ($Kn \to \infty$) and DSMC ($Kn = 20$) results are presented and are found to be in close agreement. At the earliest time $t = 0.035$ presented, a wavelike disturbance is generated at each wall and propagates into the gas layer [see Fig. 2(b)]. With increasing time [see Fig. 2(b) at $t = 0.18$], the two waves approach the middle of the slab, with their maximum amplitudes nearly unchanged. At the latest time $t = 0.4$ shown, the two waves join, forming an approximately double-in-magnitude velocity disturbance at $x = 0$.

To gain further insight into the early-time response presented in Fig. 2, we note that, at $t \ll 1$, the integrals $J_\pm^n$ and $K_\pm^n$, appearing in expressions (23)–(26) for the macroscopic fields, may be estimated by taking only the first terms on the right-hand side of Eq. (28). This is since, at these times, wall-particle interactions occur mainly with molecules whose previous boundary collisions took place before $t = 0$. When these approximations are substituted into Eq. (24), the early-time expression for the velocity

$$u(x, t \ll 1) \approx -q_w \left\{ \left(\frac{x + 1/2}{t} \right)^2 \exp\left[-\left(\frac{x + 1/2}{t} \right)^2 \right] + \left(\frac{x - 1/2}{t} \right)^2 \exp\left[-\left(\frac{x - 1/2}{t} \right)^2 \right] \right\}$$

(46)

is obtained. In practice, this result is identical to the full collisionless solution [i.e., where the full expressions (28) for $J_\pm^n$ and $K_\pm^n$ are applied] at the times presented in Fig. 2. The above approximation is similar to the collisionless response of a gas in a slab to a sudden jump in the temperature of
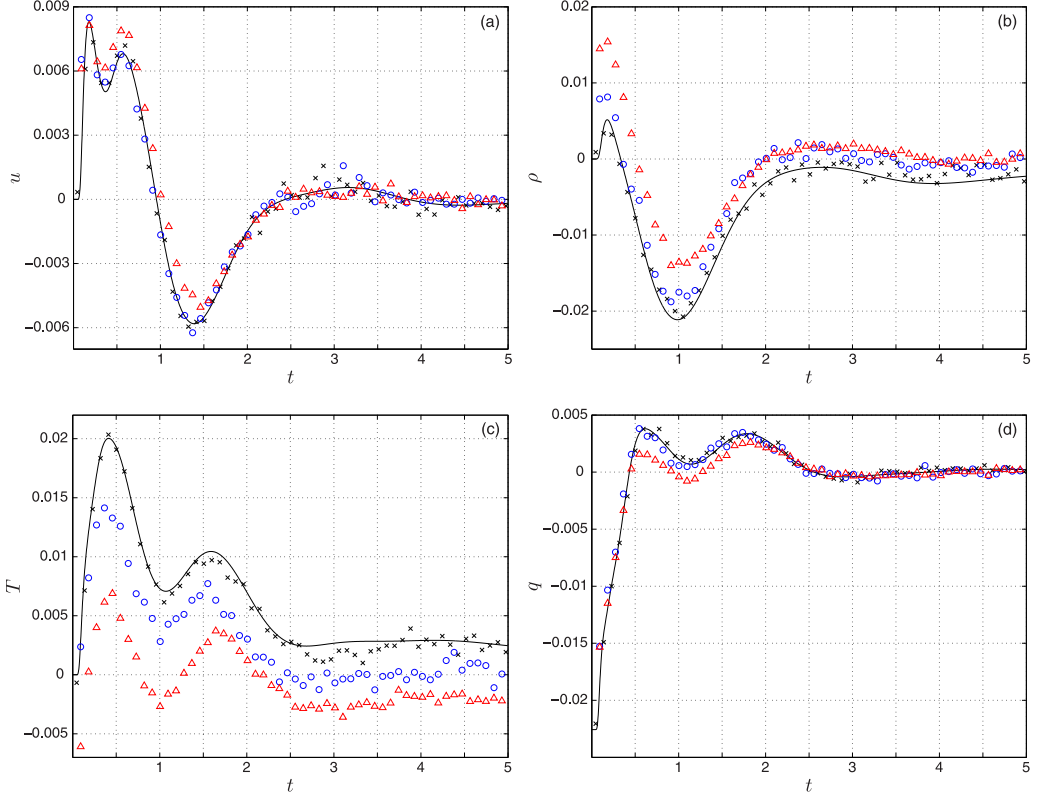
FIG. 3. Time variations of the (a) normal velocity, (b) density, (c) temperature, and (d) normal heat-flux perturbations for Kn $\gg 1$ and $q_w \ll 1$ at $x = -0.32$: comparison between collisionless solution (solid lines) and DSMC predictions for Kn = 20 (crosses), Kn = 5 (blue circles), and Kn = 1 (red triangles) with $q_w = -0.04/\sqrt{\pi}$.

its boundaries [9], and the two results become identical when expressing q_w in terms of the initial change in the temperature of the $x = -1/2$ boundary, $T_+(t = 0)/\sqrt{\pi}$ [see Eq. (16)]. This is since, as discussed in Fig. 1, the walls exhibit instantaneous change in their temperatures at $t = 0$, which remains nearly constant at early times. Based on Eq. (46), the waves generated by wall insulation propagate with the mean thermal speed (with their wave fronts located at $x = t \mp 1/2$) and their constant magnitudes are $\approx |q_w e^{-1}|$.

In difference from the early-time response, the effect of wall collisions with particles whose recent boundary collision occurred after $t = 0$ becomes more pronounced with increasing t. At this stage, the walls turn nonisothermal (see Fig. 1) and the above estimation becomes invalid. To assess the entire transient behavior of the system, Fig. 3 presents the collisionless time variations of gas velocity, density, temperature, and heat-flux perturbations at a fixed point ($x = -0.32$) and for $q_w = -0.04/\sqrt{\pi}$. The results are compared with DSMC predictions for Kn = 20, 5, and 1.

Starting with the collisionless response, we observe that all fields exhibit a short initial time interval where their $t < 0$ equilibrium values (17) remain unchanged. This reflects the time it takes for the signal generated at the $x = -1/2$ wall to propagate to the fixed point considered, $x = -0.32$. At later times, the velocity field shows a double-peak response, caused by the two wave fronts passing through the fixed point: the first, at earlier time, generated at $x = -1/2$, and the second, at later time (and weaker in magnitude), started at $x = +1/2$. The system then undergoes a series of time-decaying waves and achieves its final equilibrium (20) at $t \approx 5$. Within the transient period, the velocity remains $\lesssim O(10^{-2})$ (in mean thermal speed units). The maximum velocity, achieved in the
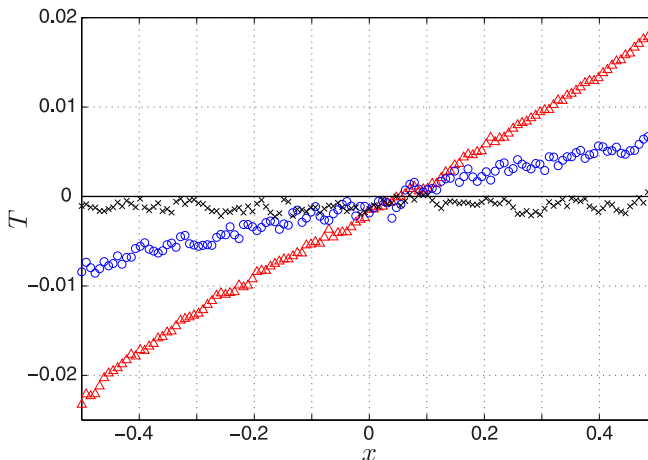
FIG. 4. DSMC-calculated temperature perturbation at the initial pure-conduction state for $q_w = -0.04/\sqrt{\pi}$ and Kn = 20 (crosses), Kn = 5 (blue circles), and Kn = 1 (red triangles). The solid line shows the $T = 0$ collisionless result.

middle of the slab (cf. Fig. 5), is $u_{max} \approx 0.0166$ and is linearly dependent on q_w, as long as the linear regime, assuming small initial temperature difference between the walls, is in effect (see Sec. V).

Comparing between collisionless and DSMC results in Fig. 3, we note that, while the agreement with the Kn = 20 data is satisfactory, considerable differences are observed, at all times, for Kn $\lesssim$ 5. This might seem peculiar, as it would have been expected that for Kn $\gtrsim$ 1 the collisionless analysis should yield a reasonable approximation when $t \lesssim$ Kn. To rationalize these discrepancies, we recall that the system response also depends on its initial-state (at $t = 0^-$) distribution. Thus, while the collisionless analysis assumes that at $t = 0^-$ the uniform conditions (17) prevail, this turns inaccurate already at Knudsen numbers of Kn $\lesssim$ 10 [17]. To demonstrate that, Fig. 4 presents the DSMC-calculated temperature perturbations of the gas at the initial pure-conduction state, for the same values of Kn as in Fig. 3. Indeed, at Kn = 20 the uniform distribution $T = 0$ is reasonably approximated. However, at Kn = 5, and to a more significant extent, at Kn = 1, the initial temperature exhibits a distinct nonzero gradient. It is therefore the deviation from the initial collisionless conditions, rather than the effect of molecular collisions for $t > 0$, that causes the breakdown of the collisionless description already at Kn $\lesssim$ 10.

Traversing to the continuum limit of small Kn, Fig. 5 presents the time variations of the macroscopic perturbations for $q_w = -8.6 \times 10^{-3}$ and Kn = 0.05. Linearized Navier-Stokes and DSMC predictions are compared at the fixed point $x = -0.32$. The results closely agree, apart from at late times close to the final equilibrium, where the signals are vanishingly small and the statistical scatter in DSMC data becomes significant. Any other (however small) discrepancies between the results may be attributed to the relatively large value of Kn chosen and vanish at lower Kn. The rapid oscillations obtained at $t \approx 0$ in the velocity field at the Navier-Stokes calculation are an artifact of the Fourier transform calculation, where high-frequency components are numerically truncated, and should be ignored.

Starting at $t < 0$, we note that the initial pure-conduction state of the system (44) is well captured by the continuum-limit scheme. Slightly after boundaries insulation, the wave generated at $x = -0.5$ reaches $x = -0.32$ and the system transient response follows a series of decaying oscillations, until the final equilibrium (45) is reached. In difference from the collisionless response (cf. Fig. 3), the time for equilibrium is longer in the continuum limit, as a result of the longer relaxation process required by molecular collisions. This time becomes prohibitively long at smaller Kn, thus inhibiting a full description using the DSMC scheme.
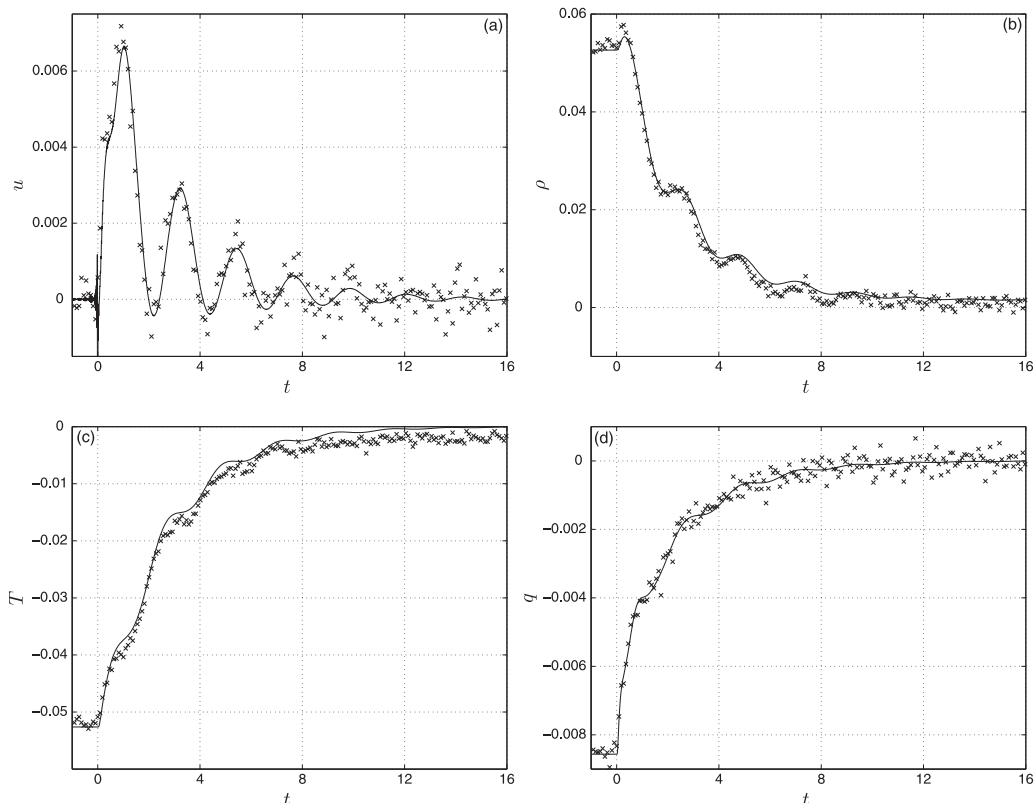
FIG. 5. Time variations of the (a) normal velocity, (b) density, (c) temperature, and (d) normal heat-flux perturbations for Kn ≪ 1 and q_w ≪ 1 at $x = -0.32$: comparison between continuum-limit solution (solid lines) and DSMC predictions (crosses) for Kn $= 0.05$ and $q_w = -8.6 \times 10^{-3}$.

To assess the overall effect of gas rarefaction on the flow magnitude in the slab, Fig. 6(a) shows the variation of the maximal flow velocity $\tilde{u}_{\max}$ with Kn for $\tilde{q}_w = -0.01/\sqrt{\pi}$. Here we define

$$\tilde{u}_{\max} = \frac{u_{\max}}{T_c^{1/2}}, \quad \tilde{q}_w = \frac{q_w}{T_c^{3/2}} \tag{47}$$

to be the maximal flow velocity and initial heat-flux magnitude scaled by the initial temperature T_c^* of the $x = -1/2$ wall (see Sec. II).[2] Owing to problem symmetry, the maximal velocity occurs at the middle of the slab. The definition (47) facilitates the comparison between systems at different Kn, by ensuring that, for each Kn, the gas is subject to the same amount of initial heat flux. This definition is also applied in following discussion of the nonlinear problem (see Figs. 9 and 10).

The imposition of equal $\tilde{q}_w$ at different Knudsen numbers results in different initial temperature differences between the walls. This is illustrated in Fig. 6(b), where the counterpart Kn variation of the initial wall temperature ratio

$$R_T = T_h^*/T_c^* \tag{48}$$

---

[2]Hereafter, quantities denoted by tildes have been rescaled by the temperature T_c^*, instead of the scale T_0^* used before.
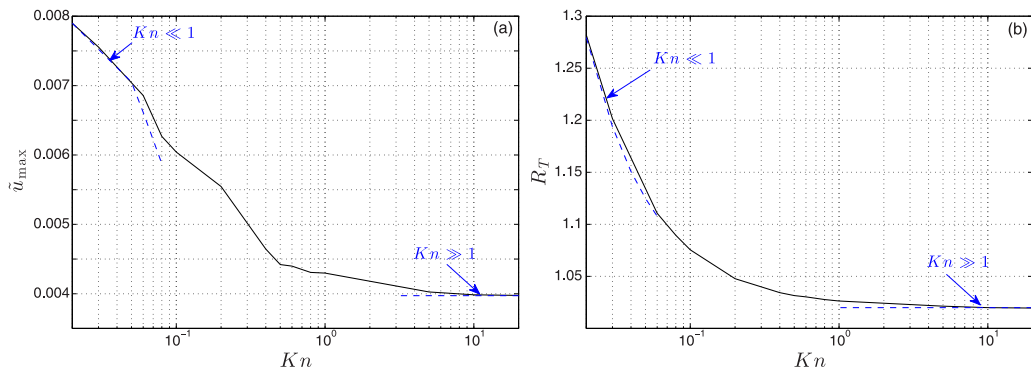
FIG. 6. (a) Variation of the maximal velocity $\tilde{u}_{\max}$ with Kn for $\tilde{q}_w = -0.01/\sqrt{\pi}$. The solid line shows DSMC results and the dashed blue lines present limit-case predictions for Kn $\ll$ 1 (continuum) and Kn $\gg$ 1 (collisionless). (b) Variation with Kn of the walls temperature ratio R_T at initial equilibrium for $\tilde{q}_w = -0.01/\sqrt{\pi}$. The solid line shows DSMC data and the dashed blue lines present limit-case results for Kn $\ll$ 1 (continuum) and Kn $\gg$ 1 (collisionless).

is presented. Here T_h^* is the initial temperature of the $x = 1/2$ wall. For the linear assumption to be valid, the condition $R_T - 1 \ll 1$ should be satisfied. The solid lines in Fig. 6(b) show DSMC results and the dashed lines present limit-case predictions for continuum and collisionless conditions.

Starting with Fig. 6(a), we note that, at fixed $\tilde{q}_w$, the maximum velocity is monotonically decreasing with Kn. This is since, for constant $\tilde{q}_w$, the initial temperature ratio R_T, a measure of the total energy captured by the system at $t = 0$, decreases with Kn [see Fig. 6(b)]. In the continuum limit, the decrease in R_T is well predicted by the Kn $\ll$ 1 asymptote, reflecting the inverse Kn dependence of the temperature ratio on the heat flux [see Eq. (30)]. For the present choice of $\tilde{q}_w = -0.01/\sqrt{\pi}$, the maximal flow speed varies between $\tilde{u}_{\max} \approx 7.9 \times 10^{-3}$ at Kn $= 0.02$ and $\tilde{u}_{\max} \approx 4 \times 10^{-3}$ for collisionless conditions. The two limits are captured by the low- and high-Kn asymptotes, which also indicate that the Navier-Stokes and collisionless schemes break down for Kn $\gtrsim 0.05$ and Kn $\lesssim 10$, respectively. In addition, the continuum scheme breaks down at Kn < 0.02, owing to the initial nonsmall temperature differences obtained [see Fig. 6(b)]. This is the reason for the slight deviations in Fig. 6(a) between the solid line and the Kn $\ll$ 1 asymptote close to Kn $= 0.02$ (see also Fig. 10).

V. NONLINEAR PROBLEM

A. Initial and final equilibrium

Having studied the linearized problem, we now turn to consider the nonlinear regime, where the initial equilibrium is characterized by large temperature differences between the walls. Hereafter, we adopt the scaling introduced in Eq. (47) and normalize the temperature by the $x = -1/2$ wall temperature. In difference from the linearized problem, the hydrodynamic fields to be presented are the total fields and not the perturbations over their mean values. While analytical predictions of the transient system response are prohibitive in this case, closed-form expressions can be found for the initial and final states.

Starting with the collisionless limit, the macroscopic fields at the initial pure-conduction state are given by the uniform distributions [16]

$$\rho(x, t < 0) = 1, \quad \tilde{T}(x, t < 0) = \tilde{p}(x, t < 0) = \sqrt{R_T},$$

$$\tilde{q}(x, t < 0) = \tilde{q}_w = \frac{1}{4\sqrt{\pi}} \frac{\gamma + 1}{\gamma - 1} \frac{\sqrt{R_T}}{\sqrt{R_T} + 1}(R_T - 1), \tag{49}$$

which degenerate to the linearized approximation (17) for the perturbations in the limit $R_T - 1 \ll 1$. Unlike in the linearized case, the gas temperature here $\sqrt{R_T}$ is lower than the arithmetic mean of initial wall temperatures $(1 + R_T)/2$. This is since, at any given time, the density of molecules reflected from the cold wall is larger than the density of those reflected from the hot wall, as their mean speed is lower. The final equilibrium in the collisionless limit is given by

$$\rho(x,t \gg 1) = 1, \quad \tilde{T}(x,t \gg 1) = \tilde{p}(x,t \gg 1) = \sqrt{R_T}, \quad \tilde{q}(x,t \gg 1) = 0, \tag{50}$$

which differs from the linearized approximation (20) by the values of the temperature and pressure.

In the continuum limit, the nonuniform initial state of the system is governed by the heat-conduction equation

$$\frac{d}{dx}\left(k(\tilde{T})\frac{d\tilde{T}}{dx} \right) = 0, \tag{51}$$

where $k(\tilde{T}) = \sqrt{\tilde{T}}$ is the nondimensional heat-flux coefficient for a hard-sphere gas [19]. Integration of Eq. (51) in conjunction with the constant heat-flux condition $\tilde{q} = \tilde{q}_w$ yields

$$\tilde{T}(x,t < 0) = \left(-\frac{3\tilde{q}_w}{2\beta}x + C \right)^{2/3}, \tag{52}$$

which is different from the linear distribution (44) obtained for $R_T - 1 \ll 1$. The constant of integration C is calculated numerically by applying the temperature jump condition

$$\tilde{T}(x = -1/2) = 1 + \tau\frac{d\tilde{T}}{dx}\bigg|_{x=-1/2}, \tag{53}$$

where $\tau = 2.1269\text{Kn}$ is the temperature jump coefficient for a hard-sphere gas [19]. At the initial equilibrium, the momentum equation in the x direction fixes the pressure to be constant,

$$\tilde{p}(x,t < 0) = \alpha, \tag{54}$$

and the density is given by

$$\rho(x,t < 0) = \alpha\left(-\frac{3\tilde{q}_w}{2\beta}x + C \right)^{-2/3}. \tag{55}$$

The constant α is determined through a normalization condition

$$\alpha = \left[\int_{-1/2}^{1/2} \left(-\frac{3\tilde{q}_w}{2\beta}x + C \right)^{-2/3} dx \right]^{-1}. \tag{56}$$

The final equilibrium state at Kn $\ll$ 1 is the uniform distribution

$$\rho(x,t \gg 1) = 1, \quad \tilde{T}(x,t \gg 1) = \tilde{p}(x,t \gg 1) = \alpha, \quad \tilde{q}(x,t \gg 1) = 0. \tag{57}$$

For later reference we note that, at the initial equilibrium for Kn $\ll$ 1, the walls' heat flux and temperature ratio are related through

$$R_T = \left(-\frac{3\tilde{q}_w}{4\beta} + C \right)^{2/3} - \frac{\tilde{q}_w\tau}{\beta}\left(-\frac{3\tilde{q}_w}{4\beta} + C \right)^{-1/3}. \tag{58}$$

The above initial and final equilibrium states have been validated numerically in the Kn $\gg$ 1 and Kn $\ll$ 1 limits using DSMC calculations. This is illustrated in Fig. 7, by comparison between DSMC and analytical predictions for the initial distributions of temperature [Fig. 7(a)] and density [Fig. 7(b)] at $R_T = 10$. The overall agreement is satisfactory. Slight deviations are observed close to the walls in the Kn = 0.02 solution, where the effect of Knudsen layers, magnified by the relatively large gradients of the hydrodynamic fields (and hence increase in the local Knudsen number), is
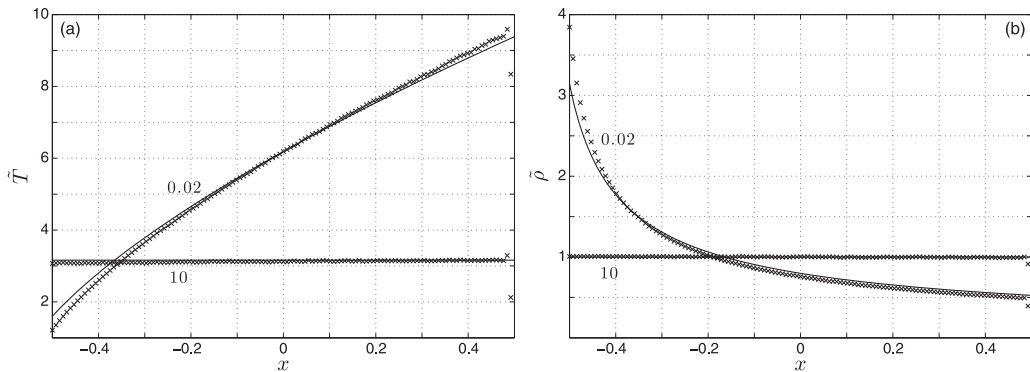
FIG. 7. Initial pure-conduction distributions of the (a) temperature and (b) density fields for $R_T = 10$ and the indicated values of Kn: comparison between DSMC (crosses) and continuum- and collisionless-limit (solid lines) results.

significant. The results obtained for the initial and final equilibria will be now used to analyze the transient system behavior.

B. Transient response

To investigate the transient gas response for nonlinear conditions, Fig. 8 presents the time variations, at a fixed point $x = -0.32$, of the normal velocity and heat flux for $R_T = 10$ and different values of the Knudsen number: large (Kn = 20) [Figs. 8(a) and 8(b)] and small (Kn = 0.02) [Figs. 8(c) and 8(d)]. The results are based on DSMC calculations. A comparison is made with the initial equilibrium values predicted by Eqs. (49) and (58).

Although the initial state of the system is characterized by large temperature gradients, the findings in Fig. 8 appear qualitatively similar, in terms of disturbance waveform, to those presented in the linearized regime [cf. Figs. 3(a), 3(d), 5(a), and 5(d)]. Similarly, the system equilibration time remains nearly unchanged by the difference in the initial conditions, indicating that the time required for system relaxation is affected mainly by the Knudsen number. The single significant difference between the results is in the order of magnitude of the hydrodynamic perturbations, being nearly two orders magnitude larger in the nonlinear case. The initial equilibrium state, which is well predicted by the dashed line in the high-Kn results in Fig. 8(b), is somewhat overpredicted (in absolute value) in Fig. 8(d). This reflects the inaccuracy in the continuum-limit scheme for nonlinear conditions, as discussed in Fig. 7.

Focusing on the effect of large initial temperature differences on the flow magnitudes obtained, Fig. 9 compares the Kn variations of the maximal speed $\tilde{u}_{\max}$ at nonlinear ($R_T = 10$) [Fig. 9(a)] and linear ($R_T = 1.1$) [Fig. 9(b)] regimes. The results in Fig. 9(b) are, in a sense, equivalent to those presented in Fig. 6(a), only that the Kn variation of $\tilde{u}_{\max}$ is given in the latter for fixed $\tilde{q}_w$ and not for fixed R_T. Here we adopt the fixed-R_T presentation, for which the restriction to linear or nonlinear conditions is easily perceived [see Fig. 6(b)]. Explicit formulas connecting R_T and q_w at Kn $\gg 1$ and Kn $\ll 1$ are given in Eqs. (49) and (58), respectively.

The results in Figs. 9(a) and 9(b) indicate a similar trend, that is, a monotonic increase in the maximal velocity $\tilde{u}_{\max}$ with increasing Kn. This does not contradict the monotonically decreasing curve at fixed $\tilde{q}_w$ shown in Fig. 6(a), since, at constant $\tilde{q}_w$, the temperature ratio becomes increasingly large with decreasing Kn [see Fig. 6(b)]. Considering the fixed value of R_T as a measure for the system's initial energetic strength, it is expected that, when translated into kinetic energy, gas velocity becomes larger at higher Kn, where molecular collisions are less frequent.

Perhaps the most interesting feature in Fig. 9 is the ratio between the maximal velocities obtained for nonlinear and linear conditions. While the values of $\tilde{u}_{\max}$ for $R_T = 10$ are considerably larger
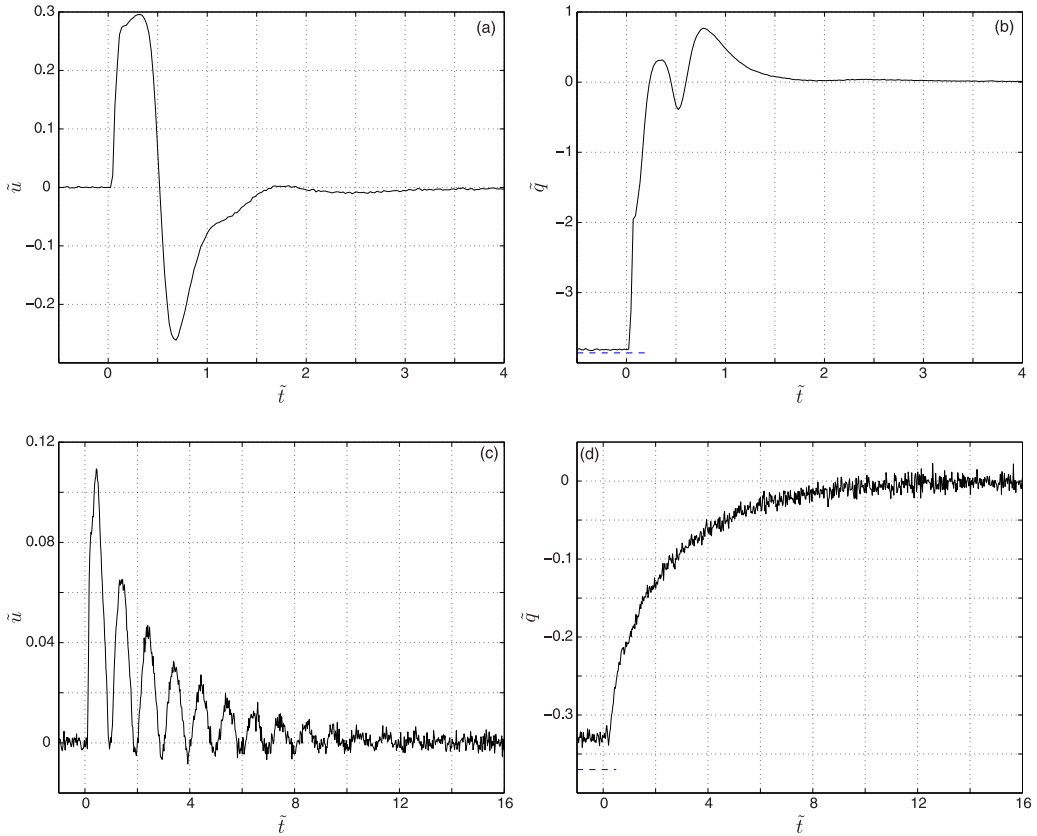
FIG. 8. Time variations of the normal velocity [(a) and (c)] and normal heat flux [(b) and (d)] at $x = -0.32$ for $R_T = 10$ and Kn = 20 [(a) and (b)] and Kn = 0.02 [(c) and (d)]. The solid lines show DSMC results and the dashed blue lines in (b) and (d) mark initial equilibrium values as predicted by Eqs. (49) and (58), respectively.
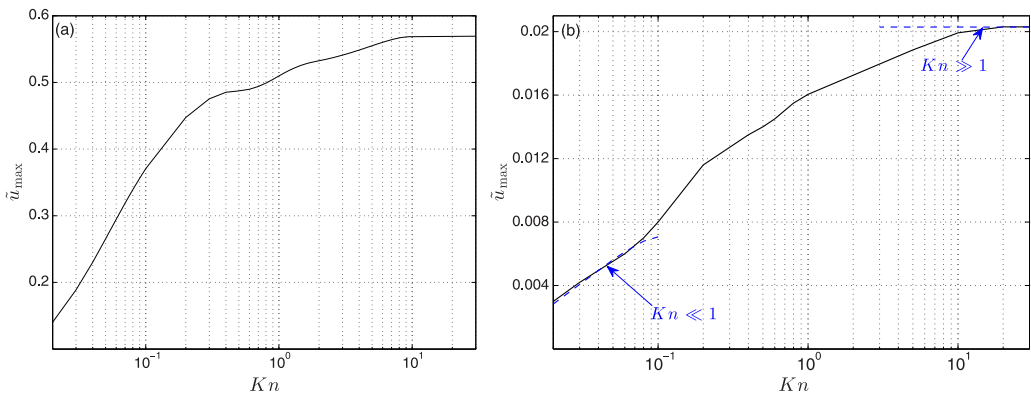

FIG. 9. Variation of the maximal velocity $\tilde{u}_{max}$ with Kn for (a) $R_T = 10$ and (b) $R_T = 1.1$. The solid lines show DSMC results and the dashed blue curves in Fig. 9(b) present limit-case predictions for Kn $\ll$ 1 (continuum limit) and Kn $\gg$ 1 (collisionless limit) in the linear case.
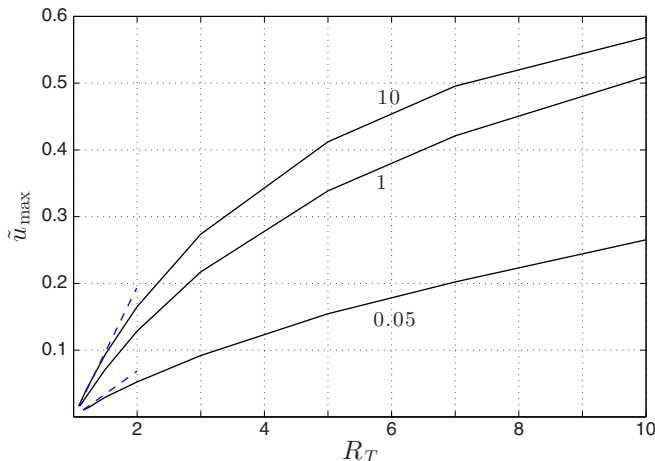
FIG. 10. Variation of the maximal velocity $\tilde{u}_{max}$ with R_T at the indicated values of Kn = 0.05, 1, and 10. The solid lines show DSMC results and the dashed blue lines present limit-case predictions for $R_T - 1 \ll 1$ at Kn = 0.05 (continuum limit) and Kn $\gg$ 1 (collisionless).

than for $R_T = 1.1$ [as also observed by comparing Figs. 8(a), 8(c), 3(a), and 5(a)], they are much smaller than expected by the quotient $(10 - 1)/(1.1 - 1) = 90$, which is the ratio between the values of $R_T - 1$ at $R_T = 10$ and $R_T = 1.1$. Specifically, $\tilde{u}_{max}$ does not exceed $\tilde{u}_{max} = 0.6$ in thermal-speed units for collisionless conditions. It is therefore observed that nonlinear effects reduce the efficiency of flow generation through boundaries insulation. For collisionless conditions, this is attributed to the initial equilibrium state (49), in which the gas temperature $\sqrt{R_T}$ is lower than the arithmetic mean of the initial wall temperatures. As stated in Sec. V A, this results from the microscopic state of the gas, where the gas molecules reflected from the cold wall are slower and therefore larger in number. For continuum conditions, the reduced efficiency may be related to the mechanism of thermal dissipation, absent in the linear regime. This assertion, however, requires further study of the nonlinear continuum equations (where a nonlinear dissipation term appears in the energy balance), which has not been carried out in the present work.

To complement the discussion of the nonlinear problem, Fig. 10 presents the variation of $\tilde{u}_{max}$ with R_T at several values of Kn, based on DSMC calculations. The dashed lines added to the Kn = 0.05 and Kn = 10 curves show a comparison with linearized limit-case predictions for continuum and collisionless conditions, respectively. In agreement with Fig. 9, the results in Fig. 10 indicate an increase in $\tilde{u}_{max}$ with both R_T and Kn. The breakdown of the linear description may be assessed through a comparison of the dashed and solid lines at Kn = 0.05 and Kn = 10, showing that the linear approximation becomes invalid for $R_T \gtrsim 1.3$ (cf. discussion of Fig. 6). At these values of R_T, nonlinear effects become significant and result in attenuation of the flow field magnitude below the value predicted by linear theory.

VI. CONCLUSION

We studied the time response of a gas in a micro-slab, set at the initial pure-conduction state, to instantaneous thermal insulation of its boundaries. The problem was analyzed in the whole range of gas rarefaction rates and for arbitrary initial temperature differences between the walls. Analytical solutions were derived for linearized conditions of small temperature differences in the limits of large (collisionless) and small (continuum) Knudsen numbers. These solutions were supported by direct simulation Monte Carlo calculations, which were then applied to investigate the nonlinear problem of large initial temperature differences. Followed by the system's initial state, the results describe the transient gas response to boundaries insulation, which includes a series of time-decaying

waves, propagating across the slab, and transferring the system between its conductive and adiabatic equilibria. While large initial temperature differences result in growing flow rates, it is found that nonlinear effects reduce the efficiency of insulation-induced flow generation. At high Knudsen numbers, this is rationalized through the initial system state, where the gas uniform temperature is lower than the arithmetic mean of wall temperatures. At low Knudsen numbers, the dominant effect of molecular collisions is likely to cause thermal dissipation, resulting in inevitable energy losses.

The agreement between the DSMC and analytical limit-case predictions was generally satisfactory. Yet the breakdown of the limit-case schemes was observed, in several cases, earlier than expected. To begin with, the collisionless description in the linear case becomes invalid at Knudsen numbers as large as Kn $\lesssim$ 10. This is since, already at rather large Knudsen numbers, the initial pure-conduction state of the system deviates considerably from the collisionless description. In a different context, the continuum-limit predictions for the pure-conduction state appear inaccurate at nonlinear conditions, where the effect of Knudsen layers, magnified by the relatively large gradients of the hydrodynamic fields (and hence increase in the local Knudsen number), becomes significant.

The present work focused on the unsteady transient response of the gas system to instantaneous boundaries insulation. Yet the analysis may be readily applied to calculate the gas response to any arbitrary time history of the boundary-imposed heat flux. As such, the flow generated through wall heat-flux control may prove to be a useful means for exciting microscale gas flows with no moving parts. As an advantage over the specification of boundary temperature, routinely imposed in theoretical studies of rarefied gas flows, application of heat-flux boundary conditions may be directly implemented in a practical setup. The study of more elaborate two- and three-dimensional configurations, as well as different types of microscopic boundary conditions (other than the diffuse-reflecting boundaries considered here), is deferred to future work.

---

[1] G. Karniadakis, A. Beskok, and N. Aluru, *Microflows and Nanoflows: Fundamentals and Simulation* (Springer, New York, 2005).

[2] N.-T. Nguyen, X. Huang, and T. Chuan, MEMS-micropumps: A review, J. Fluids Eng. **124**, 384 (2002).

[3] N.-T. Nguyen and Z. Wu, Micromixers–A review, J. Micromech. Microeng. **15**, R1 (2005).

[4] F. Amirouche, Y. Zhou, and T. Johnson, Current micropump technologies and their biomedical applications, Microsyst. Technol. **15**, 647 (2009).

[5] J. Maxwell, On stresses in rarefied gases arising from inequalities of temperature, Philos. Trans. R. Soc. London **170**, 231 (1879).

[6] J. Chen, S. Stefanov, L. Baldas, and S. Colin, Analysis of flow induced by temperature fields in ratchet-like microchannels by direct simulation monte carlo, Int. J. Heat Mass Transfer **99**, 672 (2016).

[7] Y. Sone, Effect of sudden change of wall temperature in rarefied gas, J. Phys. Soc. Jpn. **20**, 222 (1965).

[8] M. Perlmutter, *Analysis of Transient Heat Transfer through a Collisionless Gas Enclosed between Parallel Plates* (ASME, New York, 1967), ASME paper 67-HT-53.

[9] A. Manela and N. Hadjiconstantinou, On the motion induced in a gas confined in a small-scale gap due to instantaneous boundary heating, J. Fluid Mech. **593**, 453 (2007).

[10] A. Manela and N. Hadjiconstantinou, Gas-flow animation by unsteady heating in a microchannel, Phys. Fluids **22**, 062001 (2010).

[11] P. Gospodinov, V. Roussinov, and S. Stefanov, Nonisothermal oscillatory cylindrical Couette gas flow in the slip regime: A computational study, Eur. J. Mech. B **33**, 14 (2012).

[12] A. Manela and L. Pogorelyuk, Cloaking via heating: Approach to acoustic cloaking of an actuated boundary in a rarefied gas, Phys. Fluids **26**, 062003 (2014).

[13] A. Manela and L. Pogorelyuk, Active noise control of a vibrating surface: Continuum and non-continuum investigations on vibroacoustic sound reduction by a secondary heat-flux source, J. Sound Vib. **358**, 20 (2015).

[14] J. Meng, Y. Zhang, and J. Reese, Numerical simulation of rarefied gas flows with specified heat flux boundary conditions, Commun. Comput. Phys. **17**, 1185 (2015).

[15] G. Bird, *Molecular Gas Dynamics and the Direct Simulation of Gas Flows* (Clarendon, Oxford, 1994).

[16] T. Gombosi, *Gaskinetic Theory* (Cambridge University Press, Cambridge, 1994).

[17] E. Gross and S. Ziering, Heat flow between parallel plates, Phys. Fluids **2**, 701 (1959).

[18] M. Kogan, *Rarefied Gas Dynamics* (Plenum, New York, 1969).

[19] Y. Sone, *Molecular Gas Dynamics: Theory, Techniques, and Applications* (Birkhäuser, Boston, 2007).